Computational Geosciences (2018) 22:833–849
https://doi.org/10.1007/s10596-018-9728-6

ORIGINAL PAPER

Optimal design of hydraulic fracturing in porous media using the phase field fracture model coupled with genetic algorithm

Sanghyun Lee[1] · **Baehyun Min**[2] · **Mary F. Wheeler**[3]

Received: 20 May 2017 / Accepted: 22 January 2018 / Published online: 10 February 2018
© Springer International Publishing AG, part of Springer Nature 2018

Abstract

We present a framework for the coupling of fluid-filled fracture propagation and a genetic inverse algorithm for optimizing hydraulic fracturing scenarios in porous media. Fracture propagations are described by employing a phase field approach, which treats fracture surfaces as diffusive zones rather than of interfaces. Performance of the coupled approach is provided with applications to numerical experiments related to maximizing production or reservoir history matching for emphasizing the capability of the framework.

Keywords Hydraulic fracturing · Phase field · Genetic algorithm · Production maximization · History matching

1 Introduction

Multistage hydraulic fracturing (i.e., fracking) has been considered the most pragmatic technology to improve the productivity of hydrocarbon-bearing shale formations since hydraulic fractures play the role of conductive conduits in tight porous media. For fracking, slickwater-containing additives (e.g., proppants and chemicals) are injected at sufficiently high rates and pressures above well fracture pressure down into a well (Fig. 1). The created fractures are kept open by the proppants, and provide increased contact between the wellbore and the shale formation, resulting in increased oil and gas production. Recent advances in hydraulic fracturing with horizontal drilling have increased the area of drainage in contact with the wellbore by six orders of magnitude [61].

Productivity of a fractured hydrocarbon-bearing formation depends on reservoir properties (e.g., permeability) and operating parameters (e.g., well locations, the number of fracturing stages, and stage spacing). A study of an optimal number of hydraulic fractures for each horizontal well at Bakken shale model was presented in [57]. It was found that increasing the density of hydraulic fractures and decreasing the fracturing spacing enhanced the productivity, in general; however, the incremental production resulting from additional fracking decreased [23]. The longer the fracture length was, the more profitable the well was; however, the revenue increment decreased due to the increase in treatment volume [10, 60]. Maximizing the net present value of a tight gas reservoir was also studied in [36].

Fractured zones are often mimicked as thin planes in which enhanced permeability values are allocated. This simplified approach might ignore interference effects among hydraulic fractures called stress shadowing. The stress-shadowing effect refers to suppression of hydraulic fractures resulting from compressive stresses exerted on them by neighboring hydraulic fractures [1, 17, 38]. If the distance between the hydraulic fractures along the well is not far enough, the propagation of those fractures is affected by the interaction between the stress around each fracture. The interferences may result a less effective fracture propagation followed by the deterioration of

✉ Baehyun Min
bhmin01@ewha.ac.kr

Sanghyun Lee
lee@math.fsu.edu

[1] Department of Mathematics, Florida State University, 208 Love Building 1017 Academic Way, Tallahassee, FL 32306-4510, USA

[2] Department of Climate and Energy Systems Engineering, Division of Sustainable Systems Engineering, Ewha Womans University, Ewhayeodae-gil 52, Seodaemun-gu, Seoul 03760, Republic of Korea

[3] Center for Subsurface Modeling, The Institute of Computational Engineering and Sciences, The University of Texas at Austin, 201 East 24th Street, Austin, TX 78712, USA

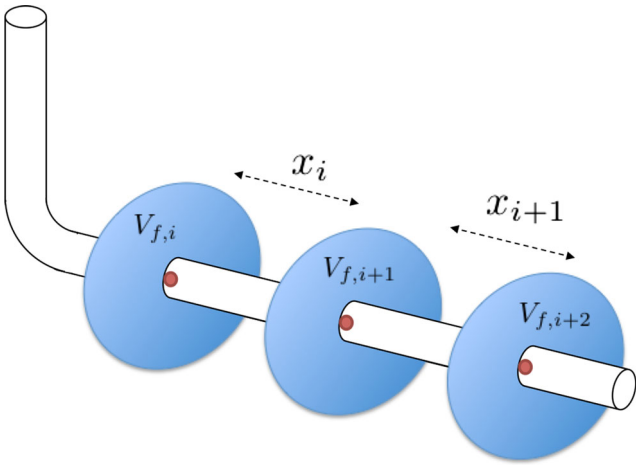

Fig. 1 Schematic of wellbore and near-wellbore of a horizontal well with multiple hydraulic fractures. Here x_i are distances between hydraulic fractures and $V_{f,i}$ are each injection sources

hydrocarbon production. In Bakken and Utica shale wells, for example, Hess Corporation [15] deployed downhole geophones to monitor microseismic events associated with multistage hydraulic fracturing and observed the stress-shadowing effect. The observation showed that closely spaced fracturing stages were interfered with one another and bounced cyclically in and out of the fractured zone. For maximizing the performance of fractured horizontal wells, it is necessary to develop a model that can simulate the propagation of multiple fractures while taking the interaction between adjacent fractures into account [12, 15, 35, 53, 65–67, 69]. Recently, Cheng et al. [12] proposed applying the C2Frac model for simulating the growth of hydraulic fractures from multiple perforation intervals in a single stage with low computational costs. The effectiveness of the C2Frac model was verified by comparing numerical solutions provided by a fully coupled planar 3D simulator ILSA [54, 55].

In this paper, we investigate the hydraulic fracturing simulation by using the variational methods and energy minimization that has been widely developed in [9, 18]. The numerical approaches for the studies are based on Ambrosio-Tortorelli elliptic functionals [4, 5]. An important numerical extension of [18] towards a thermodynamically consistent phase field fracture model has been studied in [39, 41]. In the phase field fracture approach, discontinuities in the displacement field $\mathbf{u}$ across the lower-dimensional crack surface are approximated by an indicator scalar function $\varphi \in [0, 1]$. This phase field function φ introduces a diffusive transition zone, which has a half bandwidth ε, between the fracture ($\varphi = 0$) and the un-fractured ($\varphi = 1$) material. This approach becomes as a variational inequality since the fracture propagation is required to satisfy a crack irreversibility constraint.

A crucial step to applying variational phase field fracture techniques in subsurface modeling (Biot system) has been achieved in [43]. Here, the phase field fracture has been extended to poro-elasticity in which the pressure is included. The concepts outlined in [43] have been further substantiated both theoretically and numerically in [32, 44, 46, 47]. Further studies using phase field fracture techniques treating multiphysics include [21, 29–31, 34, 37, 40, 64]. Advantages of the phase field method are that joining and branching of curvilinear paths are automatically included in the energy minimization; that is, calculating stress intensity factors and re-meshing along the crack path are embedded in the model [25]. Because the phase field fracture approach provides detailed and robust fracture propagation in heterogeneous reservoir and geomechanical parameters, and can be extended to multi physics problems [29, 30], it is important to investigate coupling techniques for optimization and history matching.

The objective of this study is to establish a numerical simulation framework by combining a phase field fracture model and an evolutionary optimization algorithm to tackle realistic scenarios. For example, the framework can be used for maximizing the productivity of multistage hydraulic fracturing at a tight shale formation by avoiding stress-shadowing effect. In particular, here, for convenience, we adopt a non-intrusive approach such as genetic algorithm as the optimization module in the framework. The performance of the coupled model is demonstrated with applications to several numerical experiments. In addition, we note that the phase field model is being integrated with a reservoir simulator for predicting flow rate. Here, as an alternative, the total volume (or total area for two dimensions) of hydraulic fractures is employed as the metric of well productivity. The relation between the production and the area of the fractures is discussed in [68].

2 Methods

2.1 Modeling of hydraulic fractures with phase field

In this section, we briefly recapitulate essential phase field fracture propagation concepts, which have been modeled and implemented in [32, 44, 46, 47].

Here, $\Lambda := \Lambda(t) \in \mathbb{R}^d$ $(d = 2, 3)$ is a smooth open and bounded computational domain with Lipschitz boundary $\partial\Lambda := \partial\Lambda(t)$. Let $[0, T]$ be the computational time interval with $T > 0$ and time is denoted by $t \in [0, T]$. As discussed in [9, 18], the fracture $\mathcal{C}(t)$ is contained compactly in $\Lambda(t)$. The displacement of the solid and diffusive flow in an un-fractured porous medium (reservoir) are modeled in $\Omega_R := \Omega_R(t) = \Lambda \backslash \bar{\mathcal{C}}(t)$ by the classical quasi-static

elliptic-parabolic Biot system for a porous solid saturated with a slightly compressible viscous fluid.

2.1.1 Geomechanics and phase field fracture equations

The constitutive equation for the Cauchy stress tensor is given as

$$\sigma^{\text{por}}(\mathbf{u}, p_R) - \sigma_0 = \sigma_R(\mathbf{u}) - \alpha(p_R - p_0)I, \quad \text{in } \Omega_R \times (0, T], \tag{1}$$

where $\mathbf{u}(\cdot, t) : \Omega_R \times [0, T] \to \mathbb{R}^d$ is the solid's displacement, $p_R(\cdot, t) : \Omega_R \times [0, T] \to \mathbb{R}$ is the pressure in the reservoir with an initial pressure p_0, $\alpha \in [0, 1]$ is the Biot coefficient, I is the identity tensor, and σ_0 is the initial stress value.

Given the effective linear elastic stress tensor as

$$\sigma_R := \sigma_R(\mathbf{u}) = \lambda(\nabla \cdot \mathbf{u})I + 2\mu e(\mathbf{u}), \tag{2}$$

the balance of linear momentum in the solid reads

$$-\nabla \cdot \sigma^{\text{por}}(\mathbf{u}, p_R) = \rho_s \mathbf{g} \quad \text{in } \Omega_R \times (0, T], \tag{3}$$

where $\lambda, \mu > 0$ are the Lamé coefficients, the linear elastic strain tensor is given as $e(\mathbf{u}) := \frac{1}{2}(\nabla \mathbf{u} + \nabla \mathbf{u}^T)$, ρ_s is the density of the solid, and $\mathbf{g}$ is the gravitational acceleration term. For simplicity, we prescribe homogeneous Dirichlet boundary conditions on $\partial\Lambda$ for the displacement $\mathbf{u}$.

To discuss the phase field fracture, we first introduce the Francfort-Marigo functional [18], which describes the energy with a fracture in an elastic medium as

$$E(\mathbf{u}, \mathcal{C}) = \frac{1}{2} \int_{\Omega_R} \sigma_R(\mathbf{u}) : e(\mathbf{u}) + G_c H^{d-1}(\mathcal{C})\, d\mathbf{x}, \tag{4}$$

where the Hausdorff measure $H^{d-1}(\mathcal{C})$ denotes the length of the fracture and is multiplied by G_c, the fracture toughness value (critical energy release rate). Extension to the energy with a fracture in a poro-elastic medium based on Biot system was derived and discussed in [32, 44, 46, 47], which is

$$E(\mathbf{u}, p, \mathcal{C}) = \frac{1}{2} \int_{\Omega_R} \sigma_R(\mathbf{u}) : e(\mathbf{u})\, d\mathbf{x} - \int_{\Omega_R} \alpha p_R \nabla \cdot \mathbf{u}\, d\mathbf{x} + G_c H^{d-1}(\mathcal{C}). \tag{5}$$

Next, we consider the global constitutive dissipation functional of Ambrosio-Tortorelli type [4, 5] to describe the $H^{d-1}(\mathcal{C})$ with the phase field function for a rate-independent fracture process. The latter was initially introduced for linear elasticity in [9, 18, 41]. We emphasize that here the fracture $\mathcal{C}(t)$ is regarded as a thin three-dimensional volume $\Omega_F(t)$, where the thickness of the crack is much larger than the pore size of porous media. The scalar-valued phase field function $\varphi(\cdot, t) : \Lambda \times [0, T] \to [0, 1]$ can be viewed as an indicator function, which introduces a diffusive transition zone ($0 < \varphi < 1$) between the fractured region (Ω_F) having $\varphi = 0$ and the un-fractured porous media (Ω_R) having $\varphi = 1$. The diffusive zone has length $\varepsilon > 0$ on each side of the fracture. The intermediate values constitute a smooth transition zone dependent upon the regularization parameter (length) ε (see Fig. 2 for more details). The boundary of the fracture is denoted by $\Gamma_F(t) := \bar{\Omega}_F(t) \cap \bar{\Omega}_R(t)$.

We assume that the effective fluid stress is given by $\sigma_F := \sigma|_{\Omega_F} = -p_F I$ and continuity of normal stresses:

$$(\sigma_R(\mathbf{u}) - \alpha p_R I) \cdot \mathbf{n}_F = -p_F \mathbf{n}_F \quad \text{on } \Gamma_F, \tag{6}$$

where $\mathbf{n}_F$ is the outward pointing normal vector of the interface Γ_F and $p_F = p|_{\Omega_F}$ is the pressure in the fracture. The leading order of the fracture fluid stress is derived from lubrication theory in [44, 47]. In addition, we use the continuity of pressures

$$p_R = p_F \quad \text{on } \Gamma_F, \tag{7}$$

and obtain

$$(\sigma_R(\mathbf{u}) - \alpha p I) \cdot \mathbf{n}_F = -p \mathbf{n}_F \quad \text{on } \Gamma_F, \tag{8}$$

by $p = p_R = p_F$. We do not distinguish between σ_R, p_R and σ_F, p_F in the global dissipation form by employing the definition of φ and the interface conditions (7)–(8). We rewrite (5) as the global formation where all definitions are extended to Λ. Then, we obtain

$$\begin{aligned} E_\varepsilon(\mathbf{u}, p, \varphi) = & \int_\Lambda \frac{1}{2}((1-\kappa)\varphi^2 + \kappa)\sigma(\mathbf{u}) : e(\mathbf{u})\, d\mathbf{x} \\ & - \int_\Lambda (\alpha - 1)\varphi^2 p \nabla \cdot \mathbf{u}\, d\mathbf{x} \\ & + \int_\Lambda (\varphi^2 \nabla p)\mathbf{u}\, d\mathbf{x} + G_c \int_\Lambda \left(\frac{1}{2\varepsilon}(1-\varphi)^2 + \frac{\varepsilon}{2}(\nabla \varphi)^2 \right) d\mathbf{x}, \end{aligned} \tag{9}$$

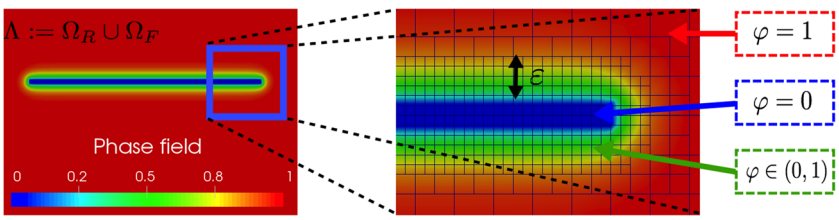

Fig. 2 An example of a fracture defined with the phase field function $\varphi \in [0.1]$

where ε is the length of the diffusive zone presented in Fig. 2 and $\kappa \ll \varepsilon$ is a small positive regularization parameter which is set to 10^{-10}.

Moreover, fracture evolutions satisfy a crack irreversibility condition that is an inequality condition in time: $\partial_t \varphi \leq 0$. Consequently, the resulting system can be characterized as a quasi-stationary (time-dependent) variational inequality, in which the continuous irreversibility constraint is approximated by $\varphi \leq \varphi^{\text{old}}$, where φ^{old} is the phase field solution at the previous time step and φ is the current solution. The phase field function is subject to homogeneous Neumann conditions on $\partial\Lambda$. The initial domains, $\Omega_F(\cdot, 0)$ and $\Omega_R(\cdot, 0)$, are defined by a given phase field value $\varphi(\cdot, 0)$.

Finally, we introduce a strong form of the Euler-Lagrangian formulation for the displacement and phase field: let p and φ be given, then find $\mathbf{u}$ such that

$$
\begin{aligned}
&-\nabla \cdot \Big(\big((1-\kappa)\varphi^2 + \kappa\big)\sigma^+ + \sigma^-\Big) \\
&+(\alpha - 1)\nabla \cdot (\varphi^2 p) + \varphi^2 \nabla p = 0 \quad \text{in } \Lambda, \mathbf{u} = 0 \\
&\quad \text{on } \partial\Lambda, (\alpha - 1)\varphi^2 p \cdot \mathbf{n} = 0 \quad \text{on } \partial\Lambda,
\end{aligned}
$$

where $\mathbf{n}$ is the outward normal vector of $\partial\Lambda$. Similarly, let $\mathbf{u}$ and p be given, then find φ such that

$$
\begin{aligned}
&\Big((1-\kappa)\sigma^+ : e(\mathbf{u})\,\varphi - G_c \varepsilon \Delta\varphi - \frac{G_c}{\varepsilon}(1-\varphi) \\
&-2(\alpha-1)\varphi p \nabla \cdot \mathbf{u} + 2\varphi \nabla p \mathbf{u}\Big) \\
&\cdot \partial_t \varphi = 0 \quad \text{in } \Lambda, \partial_{\mathbf{n}} \varphi = 0 \quad \text{on } \partial\Lambda,
\end{aligned}
$$

with a compatibility condition (which is called the Rice condition in the presence of fractures [56]),

$$
\begin{aligned}
&(1-\kappa)\sigma^+ : e(\mathbf{u})\,\varphi - G_c \varepsilon \Delta\varphi - \frac{G_c}{\varepsilon}(1-\varphi) \\
&-2(\alpha-1)\varphi p \nabla \cdot \mathbf{u} + 2\varphi \nabla p \mathbf{u} \leq 0 \quad \text{in } \Lambda, \partial_t \varphi \leq 0 \quad \text{in } \Lambda.
\end{aligned}
$$

In the discretized system, we assume $h \ll \varepsilon$, where h is the local discretization parameter.

We follow [6], where the stress tensor is additively decomposed into a tensile part $\sigma^+(\mathbf{u})$ and a compressive part $\sigma^-(\mathbf{u})$ by

$$
\begin{aligned}
\sigma^+ := \sigma^+(\mathbf{u}) = &\Big(\frac{2}{d}\mu + \lambda\Big) tr^+(e(\mathbf{u}))I + 2\mu\big(e(\mathbf{u}) \\
&- \frac{1}{d} tr(e(\mathbf{u}))I\big), \qquad (10)
\end{aligned}
$$

$$
\sigma^- := \sigma^-(\mathbf{u}) = \Big(\frac{2}{d}\mu + \lambda\Big) tr^-(e(\mathbf{u}))I, \qquad (11)
$$

respectively. Here, tr denotes the trace of the matrix and

$$
\begin{aligned}
tr^+(e(\mathbf{u})) &= \max(tr(e(\mathbf{u})), 0), \\
tr^-(e(\mathbf{u})) &= tr(e(\mathbf{u})) - tr^+(e(\mathbf{u})). \qquad (12)
\end{aligned}
$$

Note that the energy degradation only acts on the tensile part $\sigma^+(\mathbf{u})$.

2.1.2 A pressure diffraction system for modeling reservoir and fracture flow

In this section, the flow (pressure) is formulated for both reservoir and fracture as a pressure diffraction system following [32, 46]. To derive the pressure system for each sub-domain, first, we consider the two separate mass conservation equations for the fluid in the reservoir and the fracture:

$$
\partial_t(\rho_i \phi_i^\star) + \nabla \cdot (\rho_i \mathbf{v}_i) = \rho_i q_i \quad \text{in} \quad \Lambda \times (0, T], \qquad (13)
$$

where $i = F$ indicates the fracture domain Ω_F and $i = R$ indicates for the reservoir domain Ω_R. Here, $\phi_i^\star$ is the fluid fraction, where we assume $\phi_F^\star = 1$ (porosity of the fracture is one) and the reservoir fluid fraction is given as

$$
\phi_R^\star := \phi_0^\star + \alpha \nabla \cdot \mathbf{u} + \frac{1}{M}(p - p_0),
$$

where M is the Biot modulus coefficient. The velocity is given by Darcy's law

$$
\mathbf{v}_i = -\frac{K_i}{\eta_i}(\nabla p_i - \rho_i \mathbf{g}), \qquad (14)
$$

with the permeability K_i, fluid viscosity η_i for the fracture ($i = F$) and for the reservoir ($i = R$), respectively. We assume that the fluid in the reservoir and the fracture is slightly compressible: thus, we define each fluid density as

$$
\rho_i := \rho_i^0 \exp(c_i(p_i - p_i^0)) \approx \rho_i^0[1 + c_i(p_i - p_i^0)], \qquad (15)
$$

where ρ_i^0 is the reference density and c_i is the fluid compressibility. In addition, q_i is a source/sink term including leak-off [46]. The leak-off term derived in [46] (equation (2.10)) depends on the fracture opening displacement values (aperture), which affects the total volume of the fractures.

Following the general reservoir approximation with the assumption that c_R and c_F are sufficiently small, we use $\rho_R = \rho_R^0$ and $\rho_F = \rho_F^0$.

Next, in the fracture flow equation, the fracture permeability is assumed to be isotropic and has the form

$$
K_F = \frac{1}{12} w(\mathbf{u})^2, \qquad (16)
$$

as shown in [46]. Here, $w(\mathbf{u}) = [\mathbf{u} \cdot \mathbf{n}]$ denotes the aperture (width) of the fracture, which requires the computation of the jump $[\cdot]$ of the normal displacements. The corresponding details of approximating the aperture of the non-planar fractures using a level set method and interpolating these values inside the fracture are described in [33]. Non-isotropic lubrication laws have been specifically derived for fluid-filled phase field fractures in [46].

Finally, we formulate the pressure diffraction system by treating φ as an indicator function. Let φ and $\mathbf{u}$ be given, find $p(\cdot, t)$ such that

$$\rho_0 \partial_t \phi^\star + \nabla \cdot (\rho_0 K_{\text{eff}}(\nabla p - \rho_0 \mathbf{g})) = \rho_0 q, \quad \text{in } \Lambda \times (0, T], \tag{17}$$

where the coefficient functions are defined as

$$\rho_0 = \chi_{\Omega_R} \rho_R^0 + \chi_{\Omega_F} \rho_F^0, \tag{18}$$

$$\phi^\star = \phi^\star(\cdot, t) := \chi_{\Omega_R} \left(\frac{1}{M} p_R + \alpha \nabla \cdot \mathbf{u} \right) + \chi_{\Omega_F} (c_F p_F), \tag{19}$$

$$q = q(\cdot, t) := \chi_{\Omega_R} q_R + \chi_{\Omega_F} q_F, \tag{20}$$

$$K_{\text{eff}} = K_{\text{eff}}(\mathbf{u}) := \chi_{\Omega_R} \frac{K_R}{\eta_R} + \chi_{\Omega_F} \frac{K_F}{\eta_F}, \tag{21}$$

where $\chi_{\Omega_R}, \chi_{\Omega_R}$ are linear interpolation functions satisfying $\chi_{\Omega_R} = 1$ and $\chi_{\Omega_F} = 0$ in Ω_R, and $\chi_{\Omega_R} = 0$ and $\chi_{\Omega_F} = 1$ in Ω_F. In particular, once the phase field value φ is computed, we define

$$\chi_{\Omega_F} := \frac{1 - H(\varphi)}{2}, \qquad \chi_{\Omega_R} := \frac{1 + H(\varphi)}{2} \tag{22}$$

with the Heaviside function $H(\cdot)$ given as

$$H(s) = \begin{cases} 1 & \text{if } s > 0.5 + D_\varepsilon, \\ -1 & \text{if } s < 0.5 - D_\varepsilon, \\ \dfrac{s - 0.5}{D_\varepsilon} & \text{otherwise.} \end{cases} \tag{23}$$

For simplicity, we set $D_\varepsilon = 0.1$ throughout this paper.

We prescribe the boundary and interface conditions for pressure as

$$K_R(\nabla p_R - \rho_R^0 \mathbf{g}) \cdot \mathbf{n} = 0 \quad \text{on} \quad \partial\Lambda \times (0, T], \tag{24}$$

$$[p] = 0 \quad \text{on} \quad \Gamma_F \times (0, T], \tag{25}$$

$$\frac{K_R \rho_R^0}{\eta_R} (\nabla p_R - \rho_R^0 \mathbf{g}) \cdot \mathbf{n}_F = \frac{K_F \rho_F^0}{\eta_F} (\nabla p_F - \rho_F^0 \mathbf{g}) \cdot \mathbf{n}_F \quad \text{on} \quad \Gamma_F \times (0, T], \tag{26}$$

Extensions to proppant transport with non-Newtonian flow and two-phase flow in the fracture have been developed in [29, 30].

2.1.3 Global solution algorithm for phase field fracture

In Fig. 3, we present the overall algorithms for the phase field fracture propagation. First, the geomechanics-phase field system is discretized by classical continuous Galerkin linear finite element methods. Flow (pressure) equation is modeled using a locally conservative enriched Galerkin approximation approach [28]. This Biot system is coupled in time by employing the fixed stress iterative scheme which has been widely applied in [13, 26, 27, 42, 45, 58], for fractured poro-elastic media in [19, 33, 46, 59], and including multi-rate time-stepping algorithms in [2, 3].

To reduce the computational cost, we employ a predictor-corrector dynamic mesh refinement strategy developed in [22] and which was extended to three dimensions in [32, 63] with parallel high-performance computing using MPI (message passing interface). Nonlinear problems are solved using Newton's method and an analytical evaluation of the Jacobian. The constraint minimization problem is treated with a semi-smooth Newton method (i.e., a primal-dual active set method) [22]. The linear equations are solved with parallel MPI-based iterative solvers (GMRES) with block-diagonal pre-conditioning. For more details, the reader may refer to [22, 32, 33, 63]. The programming code is developed based on the open-source finite element library deal.II [7].

2.2 Optimization of hydraulic fracturing design

Most real-world engineering problems consist of multiple uncertain parameters as

$$f(\curvearrowleft) = f(x_1, x_2, \cdots, x_N), \tag{27}$$

where $f(\curvearrowleft)$ is the scalarized objective function, $\curvearrowleft$ is the vector of uncertain parameters, and N is the number of uncertain parameters. For a subsurface modeling problem, $\curvearrowleft$ may consist of reservoir properties (e.g., permeability, Poisson's ratio, and Young's modulus) or decision variables (e.g., well trajectory and number of hydraulic fractures).

Optimal design of hydraulic fracturing treatment can be defined as a maximization problem as

$$\arg \max_{\curvearrowleft \in \mathbb{R}^N} f(\curvearrowleft) = \arg \max_{\curvearrowleft \in \mathbb{R}^N} \mathbf{d}^{sim} \tag{28}$$

where $\mathbf{d}^{sim}$ is the vector of simulated subsurface responses. In this paper, $\mathbf{d}^{sim}$ is the total volume (area for two-dimensional case) of hydraulic fractures V_f, which is computed by integrating the fractured zones Ω_{Fv} obtained after running the phase field model as:

$$V_f = \int_{\Omega_{Fv}} 1 \, dA, \tag{29}$$

$$\Omega_{Fv} := \{\curvearrowleft \mid \varphi < c_v, \forall \curvearrowleft \in \Omega\}, \tag{30}$$

where c_v is the threshold used for distinguishing between fractured mesh and un-fractured mesh in the given domain. In this study, c_v is set to 0.1.

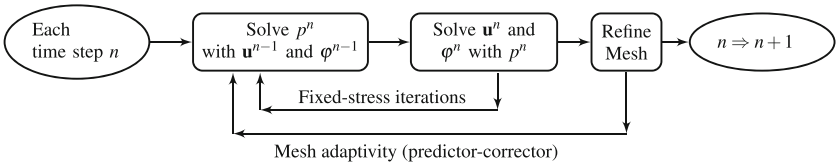

Fig. 3 Flow chart of global solution algorithm for the phase field model

Meanwhile, subsurface characterization of a fractured reservoir can be regarded as a history-matching problem that minimizes the discrepancy between $\mathbf{d}^{sim}$ and observed (i.e., actual) subsurface responses $\mathbf{d}^{obs}$ as

$$\arg \min_{\curvearrowleft \in \mathbb{R}^N} f(\curvearrowleft) = \arg \min_{\curvearrowleft \in \mathbb{R}^N} \|\mathbf{d}^{obs} - \mathbf{d}^{sim}\|. \tag{31}$$

In real-world problems, field measurements (e.g., oil production rate, water-cut, and bottom hole pressure) would compose $\mathbf{d}^{obs}$ while its corresponding $\mathbf{d}^{sim}$ would be evaluated by solving governing equations by use of a petroleum reservoir simulator. It is desirable to replace the current objective function V_f, the fracture area/volume, with hydrocarbon production rates. In other words, demonstrating the impact of detailed hydraulic fracture propagation models such as phase field for production is important and necessary for realistic field studies. However, this requires multiscale spatial and temporal coupling of the small scaled fracturing model with a large scaled reservoir simulator, calibration using field observation data, and assessing multiple questions such as staging, spacing of fractures, proppant injection, refracturing, and effects of multiple fractures. In this paper, since we focus to establish a computational framework for coupling the phase field fracture model with the optimization algorithm, we employ the optimization algorithm by optimizing the fracture area in order to show the capability of the algorithm. Coupling a production reservoir simulator with the phase field model will be treated in future works.

2.3 Genetic algorithm

Genetic algorithm (GA), a stochastic optimization approach based on the evolutionary process of natural selection [24], is adopted to search for the global optimal solution of a hydraulic fracturing problem. The advantage of this gradient-free method is to require no assumption on the form of the objective function. GA is a population-based process [20]. Qualities of populations in subsequent generations are expected to be more improved than that of the population in the current generation.

Pseudo code of the evolutionary process in genetic algorithm is described in Table 1. This iterative process performs different genetic operations on a pool of solutions. Let $\mathbb{X}^p$ and $\mathbb{X}^o$ be the parent population and the offspring population, respectively: $\curvearrowleft^p \in \mathbb{X}^p$ and $\curvearrowleft^o \in \mathbb{X}^o$. The initial parent population $\mathbb{X}^p_{t=0}$ consists of N_{pop} solutions that are generated at random or based on prior knowledge. Here, N_{pop} is the population size per generation. Each solution (i.e., individual) encodes its own vector of uncertain parameters $\curvearrowleft$ by real or binary number. In GA, the individual $\curvearrowleft$ and each element of individual x are called chromosome and gene, respectively. At each generation, $\mathbb{X}^o$ is created by recombining qualified solutions in the mating pool $\mathbb{X}^p \cup \mathbb{X}^o$. The qualified solutions of the mating pool are selected using a tournament or a roulette wheel method [20]. Note that the fitness (i.e., objective function value) of each solution in the mating pool is evaluated by running the phase field model in this study.

Recombination is sequentially invoked using two genetic operators: crossover (see Table 2) and mutation (see

Table 1 Pseudo code of the evolutionary process in genetic algorithm

1	:	**INITIALIZE** the parent population $\mathbb{X}^p_{t=0}$ with N_{pop} solutions generated based on prior knowledge or at random. The initial offspring population $\mathbb{X}^q_{t=0} = \varnothing$.
2	:	**EVALUATE** each parent solution in $\mathbb{X}^p_0$.
3	:	**while** *termination condition* is not achieved **do**
4	:	$t = t + 1$.
5	:	**SELECT** N_{pop} superior solutions from the mating pool $\mathbb{X}^p_{t-1} \cup \mathbb{X}^q_{t-1}$.
6	:	**UPDATE** the parent population $\mathbb{X}^p_t$ with the selected solutions.
7	:	**CROSSOVER** pairs of the parent solutions for creating N_{pop}-sized $\mathbb{X}^q_t$.
8	:	**MUTATE** the resulting offspring population $\mathbb{X}^q_t$.
9	:	**EVALUATE** each offspring solution in $\mathbb{X}^q_t$.
10	:	**end**

Table 2 Pseudo code of crossover to create new solutions in genetic algorithm

1	:	$i = 1$
2	:	**while** $i < N_{pop}$ **do**
3	:	**GENERATE** the random probability $P_r \in [0, 1]$
4	:	**SELECT** two parent members $\curvearrowleft_i^p$ and $\curvearrowleft_{i+1}^p$
5	:	**if** $P_r < P_c$ then
6	:	**GENERATE** the crossover point $r_c \in [1, N]$
7	:	$\curvearrowleft_i^q = \{\curvearrowleft_{i,1}^p, \cdots, \curvearrowleft_{i,r_c}^p, \curvearrowleft_{i+1,r_c+1}^p, \cdots, \curvearrowleft_{i+1,N}^p\}$
8	:	$\curvearrowleft_{i+1}^q = \{\curvearrowleft_{i+1,1}^p, \cdots, \curvearrowleft_{i+1,r_c}^p, \curvearrowleft_{i,r_c+1}^p, \cdots, \curvearrowleft_{i,N}^p\}$
9	:	**else**
10	:	$\curvearrowleft_i^q = \curvearrowleft_i^p$
11	:	$\curvearrowleft_{i+1}^q = \curvearrowleft_{i+1}^p$
12	:	**end**
13	:	$i = i + 2$
14	:	**end**

Table 3). Let P_r, P_c, and P_m be the random probability at each genetic operation, the probability of crossover, and the probability of mutation, respectively. The evolutionary process activates crossover if $P_r < P_c$ and then does mutation if $P_r < P_m$. Both P_c and P_m are specified a priori, in general. Through the paper, P_c and P_m are 0.9 and 0.1, respectively. Here, $r_c \in [1, N]$ is the crossover point that switches all genes after that point. Here, $r_m \in [1, N]$ is the mutation point at which the random variable is altered in the range of its lower and upper limits. Note that both r_c and r_m are picked at random at each genetic operation. More details on crossover and mutation can be found in [20].

The termination condition of the evolutionary process is either the achievement of a pre-specified tolerance level or the arrival on the maximum number of generations (i.e., iterations). If the maximum number of generations is N_{gen}, the maximum number of evaluations $N_{eval} = N_{gen} \times N_{pop}$. Note that the genetic algorithm tends to explore the single global-optimum having the smallest objective-sum of a minimization problem or the largest objective-sum of a maximization problem because of the one dimension of the global-objective function.

2.4 Coupling of phase field model with assisted optimization program

Phase field fracture model discussed in Section 2.1 was integrated with an optimization toolbox, namely UT-OPT (University of Texas Austin-Multiple Realization Optimizer) [52], in order to realize, run, and optimize geomechanics simulations of hydraulic fracturing. Figure 4 shows a framework of UT-OPT. UT-OPT consists of three modules: builder, genetic algorithm (GA) [20] as a global-objective optimizer, and non-dominated sorting genetic algorithm-II (NSGA-II) [14] as a multi-objective optimizer. Builder generates ASCII input data files that are imported to one of the optimization algorithms to be executed. The input files are categorized as algorithm parameters (e.g., generation number and population size); uncertain parameters (e.g., permeability, Young's modulus, and fracture spacing); response parameters that are targeted for quality check of reservoir models (e.g., volume of fracture); and watch parameters that are un-targeted for quality check (e.g., runtime). Dynamic goal programming and successive linear-objective-reduction modules are advanced

Table 3 Pseudo code of mutation to create new solutions in genetic algorithm

1	:	$i = 1$
2	:	**while** $i < N_{pop}$ **do**
3	:	**GENERATE** the random probability $P_r \in [0, 1]$
4	:	**if** $P_r < P_m$ **then**
5	:	**GENERATE** the mutation point $r_m \in [1, N]$.
6	:	**GENERATE** the random variable $\curvearrowleft_{i,r_m}^{q,*} \in [\curvearrowleft_{r_m}^{q,min}, \curvearrowleft_{r_m}^{q,max}]$ at the mutation point r_m
7	:	$\curvearrowleft_i^q = \{\curvearrowleft_{i,1}^q, \cdots, \curvearrowleft_{i,r_m-1}^q, \curvearrowleft_{i,r_m}^{q,*}, \cdots, \curvearrowleft_{i,N}^q\}$
8	:	**end**
9	:	$i = i + 1$
10	:	**end**

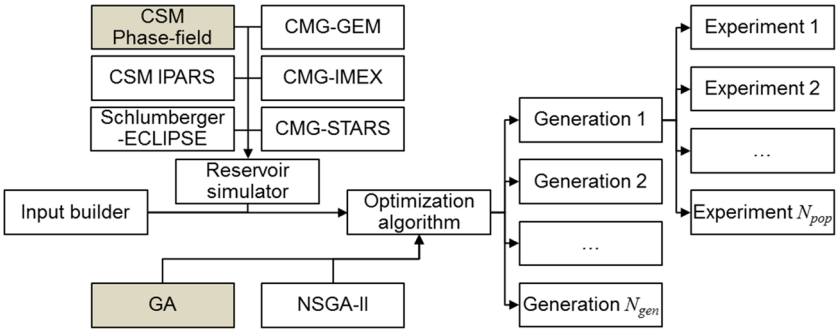

Fig. 4 Framework of the assisted optimization tool, UT-OPT

options that can be coupled with NSGA-II to improve the rate of convergence with a small loss in diversity preservation for solving a multi-objective problem in case $M > 4$ [48–50]. For reducing the computational cost associated with the generational algorithms, UT-OPT has the capability to run multiple simulations concurrently. Each simulation can be executed in high-performance parallel computing environments. Besides the phase field model, CSM's in-house simulator, namely Integrated Parallel Accurate Reservoir Simulator (IPARS) [62], and commercial reservoir simulators are linked to UT-OPT. This general-purpose optimization program can be utilized for performing sensitivity analysis, history matching, production forecasts, economic analysis, and uncertainty analysis. UT-OPT was written in C++ programming language.

3 Numerical experiments

In this section, we present three numerical examples to illustrate capabilities of the coupled algorithm. The first two examples provide maximization problems and the last demonstrates the minimization. We clarify that the domain size of each example herein is designed as lab-scale for saving computational costs accompanied with multiple phase field runs during optimization. All the examples run 20 experiments concurrently in each generation, and every phase field fracture simulation is executed with 4 parallel processors.

3.1 Example 1: Maximization of fracture area with a well in a homogeneous reservoir

In this example, given three fractures in a fixed domain Ω, find the optimal spacing that provides the largest fracture area in Ω. Let $\Omega = (0\,\mathrm{m}, 4\,\mathrm{m})^2$ with $H = L = 4$, we prescribe parallel initial cracks with half lengths $l_0 = 0.2\,\mathrm{m}$ as illustrated in Fig. 5. The initial mesh is six times locally refined around the fracture. The smallest mesh size is $h_{\min} = 0.0013\mathrm{m}$ and the regularization parameters are chosen as $\varepsilon = 2h_{\min}$. The fracture in the center is fixed at $(2 - h_{\min}, 2 + h_{\min}) \times (2 - l_0, 2 + l_0)$, but the position of left and right fractures depends on two spacings, left and right, i.e., x_1 and x_2, respectively, in each fracturing scenario (see Fig. 5). In the homogeneous media, the critical energy release rate is chosen as $G_c = 1\,\mathrm{N\,m^{-1}}$, Young's modulus is $E = 10^8$ Pa, and Poisson ratio is set to $\nu = 0.2$. The relationship to the Lamé coefficients μ and λ is given by

$$\mu = \frac{E}{2(1+\nu)}, \qquad \lambda = \frac{\nu E}{(1+\nu)(1-2\nu)}.$$

For the fluid parameters, Biot's coefficient is set as $\alpha = 1$, $M = 1 \times 10^8$ Pa, $\eta_R = \eta_F = 1 \times 10^{-3}\mathrm{Ns/m^2}$, the reservoir permeability is $K_R = 1\,\mathrm{D} \approx 1 \times 10^{-12}\,\mathrm{m^2}$, $q_F = 60$, $c_F = 1 \times 10^{-12}\,\mathrm{Pa^{-1}}$, and the density is $\rho_F^0 = 1000\,\mathrm{kg/m^3}$.

Variable vector $\curvearrowleft$ consists of fracture spacing between the inner fracture and the outer fractures: $\curvearrowleft = (x_1, x_2)$ where $x_1, x_2 \in [0.5\,\mathrm{m}, 1.5\,\mathrm{m}]$. Thus, the number of variables $N = 2$ in this example. The objective function $f(\curvearrowleft)$ of this example to be maximized takes the form of Eq. 28 as

$$\arg\max_{\curvearrowleft \in \mathbb{R}^N} f(\curvearrowleft) = \arg\max_{\curvearrowleft \in \mathbb{R}^2} \sum_{i=1}^{N_{hf}} V_{f,i}\,, \tag{32}$$

where the number of hydraulic fractures $N_{hf} = 3$.

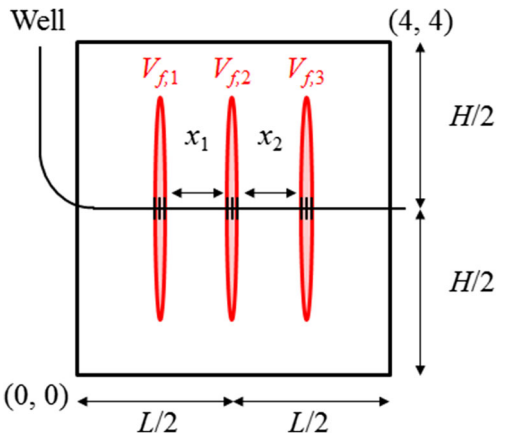

Fig. 5 Example 1. Schematic of wellbore and near-wellbore of a horizontal well with three-stage hydraulic fracturing

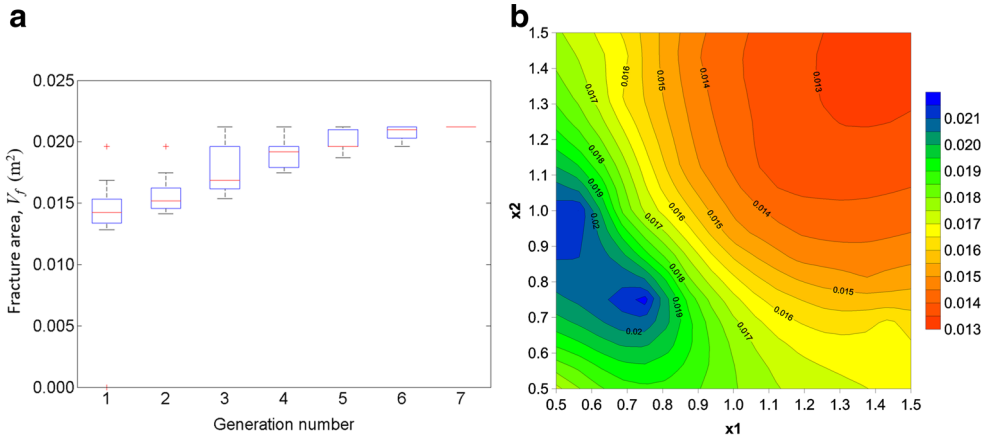

Fig. 6 Example 1. Evolution of objective function values in the homogeneous medium: **a** convergence of objective function values and **b** objective function values in variable space

Figure 6a is a boxplot to show the evolution of objective function values from the first to the seventh generations. The box in each generation consists of 20 solutions. Thus, the total number of evaluations is 140. The initial generation was created at random. The height of the box indicates the interquartile ranges (IQR) determined by the 25th and 75th percentile of the posterior solutions. The solid red line inside the box is the median of the posterior solutions. Whiskers are vertical lines above and below the box that extend to the most extreme solutions not considered outliers, while any solution regarded as an outlier is plotted as a red plus. The solutions evolve in the direction of maximizing the total area of three fractures. It appears that all solutions in the seventh generation stably converge to the global maximum, $(x_1, x_2) = (0.75\,\text{m}, 0.75\,\text{m})$. Figure 6b demonstrates the relationship between variables and objective values. Kriging was used to interpolate 140 objective function values evaluated during optimization. Homogeneity of Young's modulus in the domain delivers radial gradients of objective function values from top right corner in a two-dimensional

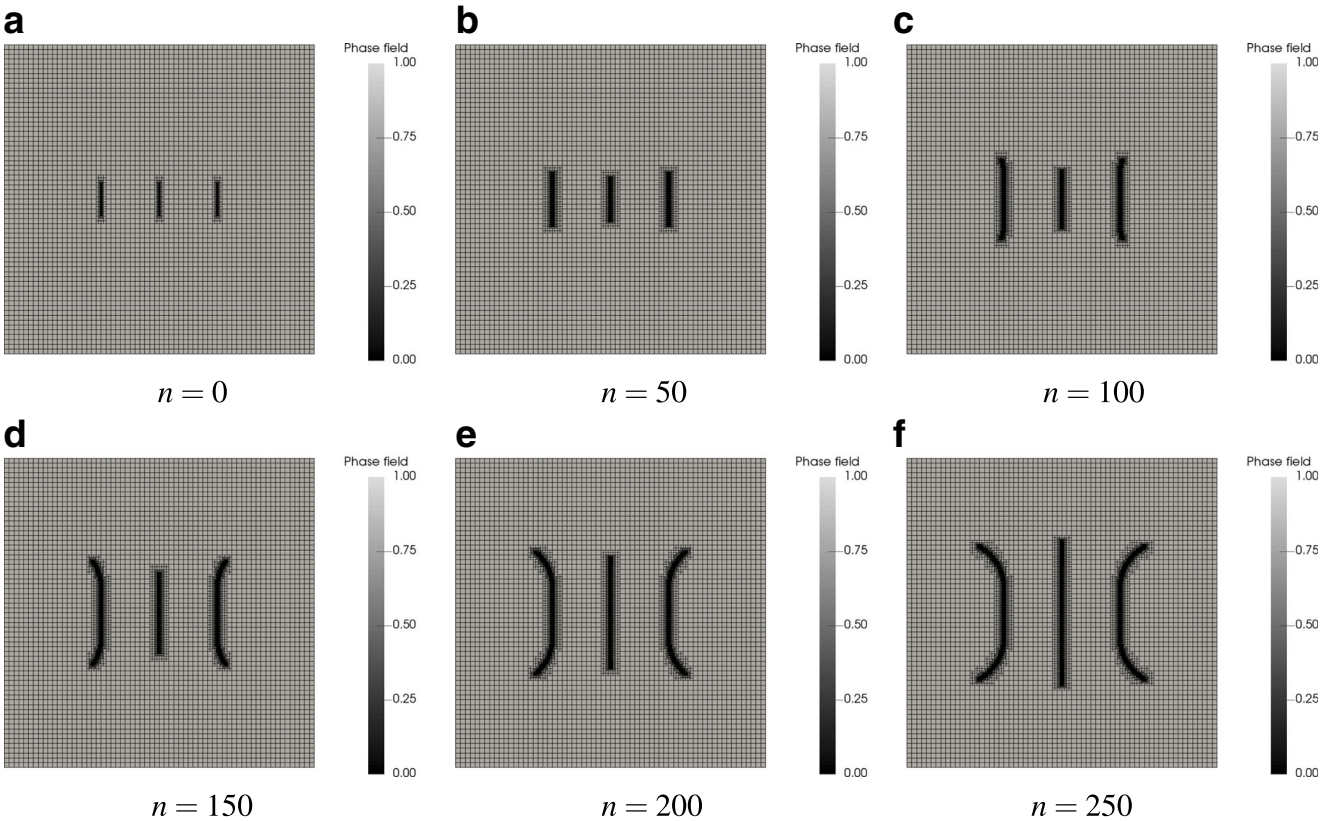

Fig. 7 Example 1. Fracture propagation of the optimal solution. Each figure illustrates the refined mesh near the fractures (which is better for visualization) for each time step. Its fracture spacing $(x_1, x_2) = (0.75\,\text{m}, 0.75,\,\text{m})$ yields $V_f = 0.0212261\,\text{m}^2$ in the homogeneous medium

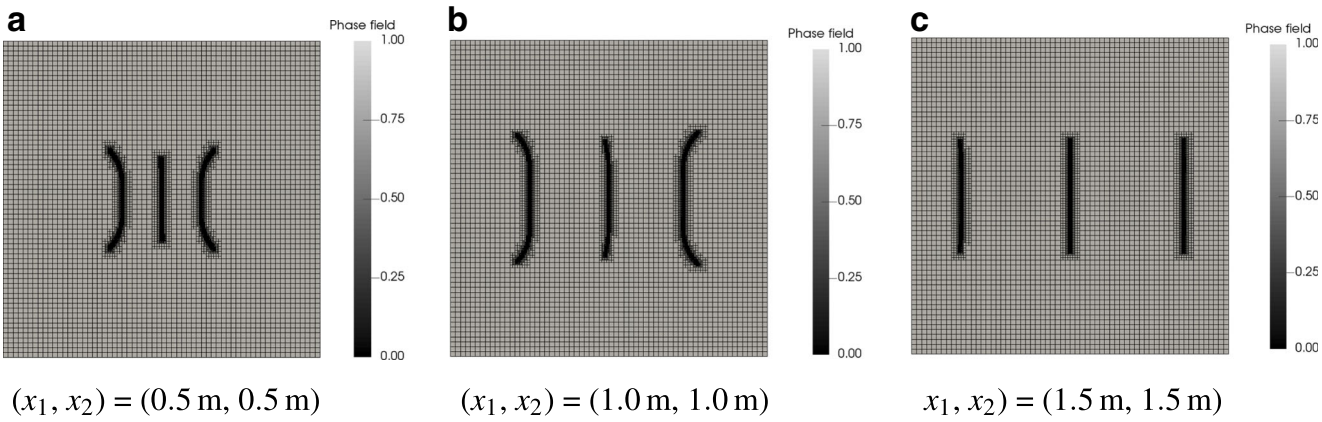

Fig. 8 Example 1. Fractures of three non-optimal solutions at time step n=250 in the homogeneous medium: **a** the closest fracture spacing $(x_1, x_2) = (0.5\,\text{m}, 0.5\,\text{m})$ yields $V_f = 0.0168475\,\text{m}^2$, **b** $(x_1, x_2) = (1.0\,\text{m}, 1.0\,\text{m})$ yields $V_f = 0.0147084\,\text{m}^2$, and **c** the farthest fracture spacing $(x_1, x_2) = (1.5\,\text{m}, 1.5\,\text{m})$ yields $V_f = 0.0128308\,\text{m}^2$

variable space. The ideal case of Fig. 6b must be symmetric because x_1 and x_2 are interchangeable. A slight asymmetry shown in Fig. 6b is due to the interpolation using Kriging from 140 evaluations. Interpolated regions where their objective values are inferred from the evaluations cause the asymmetry. We expect increasing the number of evaluations improves the degree of the symmetry. For example, adding and simulating $(x_1, x_2) = (1.0\,\text{m}, 0.5\,\text{m})$, which are not created during this optimization example, would improve the degree of the symmetry shown in Fig. 6b significantly. Note that the initial 20 evaluations are generated at random and the subsequent evaluations are done by use of crossover and mutation of their preceding solutions in GA.

In Figs. 7 and 8, the bent outer fractures and the constrained growth of the inner fracture indicate stress-shadowing effects as shown in [11] and references cited therein. Figure 7 illustrates multiple parallel fracture propagation of the global optimal solution. The optimized fracture spacing $(x_1, x_2) = (0.75\,\text{m}, 0.75\,\text{m})$ yields after 140 evaluations, the largest hydraulic fractured total area $V_f = 0.0212261\,\text{m}^2$. The stress-shadowing effects become noticeable after $n = 100$ in Fig. 7. The propagate fractures of each fracturing scenario appear to be fairly symmetric due to the spatial homogeneity of Young's modulus. Symmetry of fracture propagation is also observed in the non-optimal solutions.

Figure 8 illustrates the shape of fractures at the last time step $n = 250$. The non-optimal solutions result in smaller V_f values than that of the global-optimum. It seems that the closest fracture spacing reveals strong stress-shadowing effects resulting in the inhibition of fracture growth (see Fig. 8a), while the farthest fracture spacing reveals little stress-shadowing effect (see Fig. 8c). Note that V_f of Fig. 8c is smaller than that of Fig. 8a because the three propagated fractures in Fig. 8c are longer but thinner than those in Fig. 8a. This result arises since the fractures in Fig. 8c are isolated due to larger spacing.

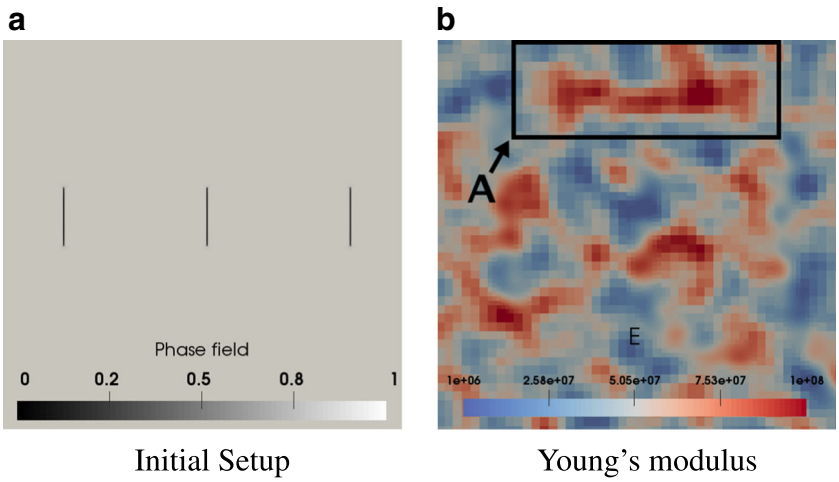

Fig. 9 Example 2. Setup: **a** parallel fractures and **b** heterogeneous E values

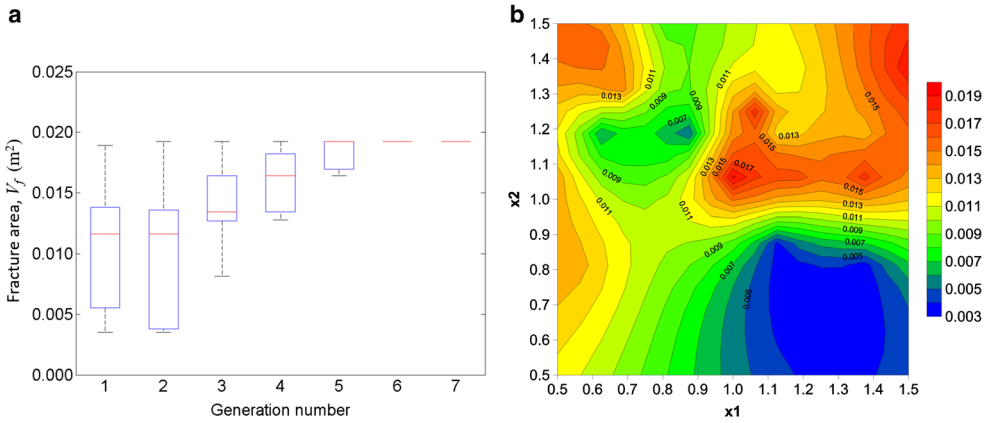

Fig. 10 Example 2. Evolution of objective function values in the heterogeneous medium: **a** convergence of objective function values and **b** objective function values in variable space

3.2 Example 2: Maximization of fracture area in a heterogeneous reservoir

In the computational domain $\Omega = (0\,\text{m}, 4\,\text{m})^2$, we set prescribed parallel initial cracks with half lengths $l_0 = 0.2\,\text{m}$ as described in Fig. 9a. The boundary conditions, initial mesh generation, fixed stress iteration tolerance, variable vector, objective function, and mechanical parameters except Young's modulus are the same as in the previous Example 1. Figure 9b shows the spatial variation of Young's modulus taking the value $E \in [10^6\,\text{Pa}, 10^8\,\text{Pa}]$. Note that a bar-shaped zone (denoted by A in Fig. 9b) having the highest Young's modulus is located in the upper middle region of the domain.

Similar to Figs. 6a and 10a shows the convergence of objective function values in the heterogeneous medium during global optimization. All solutions following the sixth generation converge on the global maximum, which appears in the second generation. The objective value of each variable vector is depicted in Fig. 10b. Because of the heterogeneity of Young's modulus, the contour lines of Fig. 10b are irregular. The optimized fracture spacing (x_1,

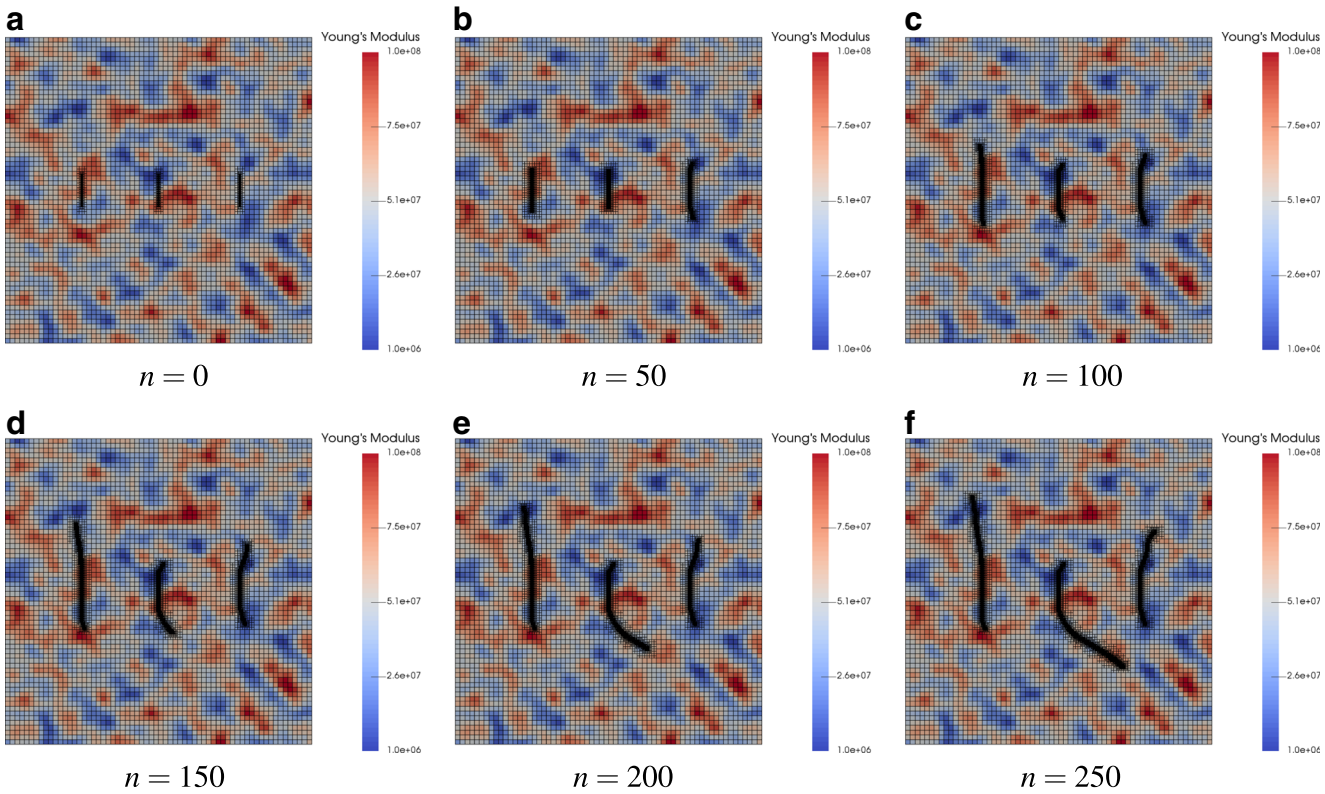

Fig. 11 Example 2. Fracture propagation of the optimal solution. Its fracture spacing $(x_1, x_2) = (1.0\,\text{m}, 1.0625\,\text{m})$ yields $V_f = 0.0192650\,\text{m}^2$ in the heterogeneous medium

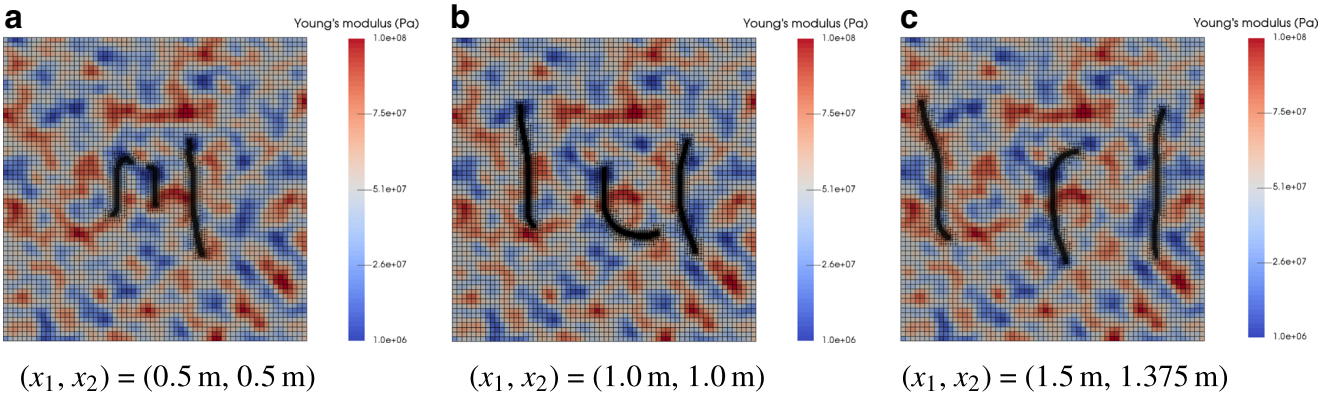

Fig. 12 Example 3. Fractures of three non-optimal solutions at time step $n = 250$ in the heterogeneous medium: **a** the fracture spacing $(x_1, x_2) = (0.5\,\text{m}, 0.5\,\text{m})$ yields $V_f = 0.0116455\,\text{m}^2$, **b** $(x_1, x_2) = (1.0\,\text{m}, 1.0\,\text{m})$ yields $V_f = 0.0182794\,\text{m}^2$, and **c** $(x_1, x_2) = (1.5\,\text{m}, 1.375\,\text{m})$ yields $V_f = 0.0189270\,\text{m}^2$

$x_2) = (1.0\,\text{m}, 1.0625\,\text{m})$ yields after 140 evaluations, the largest hydraulic fractured total area $V_f = 0.0192650\,\text{m}^2$.

Figure 11 illustrates the multiple parallel fracture propagation of the optimal solution. Compared to Fig. 7, Fig. 11 demonstrates that reservoir heterogeneity has a significant influence on fracture propagation. Each fracture tends to grow towards regions having lower Young's modulus by detouring regions having higher Young's modulus. It seems that the growth of the inner fracture to the north is suppressed by the existence of the bar-shaped zone with the highest Young's modulus in the upper middle region of the domain. The suppression is also observed in the growth of the left outer fracture to the south of the domain. Meanwhile, the bent inner fracture propagated to the southeast hinders the growth of the right outer fracture to the south. Fracture propagation results of three non-optimal solutions at the last time step $n = 250$ are illustrated in Fig. 12. Compared to Figs. 11f, 12b, and 12c, Fig. 12a having the closest perforating spacing deteriorates the fracture propagation due to the stress-shadowing effects. Figure 12c yields a similar V_f to the optimal solution.

Distinguishing the stress-shadowing effect from heterogeneity of reservoir properties remains a challenging issue. Clearly, heterogeneity would have the greatest impact on the performance of fracturing design. Nevertheless, it is necessary to consider the stress-shadowing effect is to be considered carefully for estimating a propagation path of each hydraulic fracture in heterogeneous media if operating parameters are to be determined.

3.3 Example 3: History matching

This example solves a minimization problem to explore the global minimum having the smallest discrepancy between actual (reference) and simulated areas of fractures. The actual areas of fractures were computed using the simulation results of the reference field model shown in Fig. 13. As shown in Example 1, three parallel fractures are positioned in the computational domain $\Omega = (0\,\text{m}, 4\,\text{m})^2$. All the other numerical and physical parameters are identical to those of Example 1, with an exception that a rectangle region $([2.0\,\text{m}, 3.5\,\text{m}] \times [2.5\,\text{m}, 3.0\,\text{m}])$ of which Young's modulus is largest.

The variable vector $\curvearrowleft$ of this minimization problem in Eq. 31 is set as

$$\curvearrowleft = \{x_{1,b}, x_{2,b}, y_{1,b}, y_{2,b}, E_{in}, E_{out}\}, \tag{33}$$

where $x_{1,b}$ is x-coordinate of the bottom-left corner of the bar, $x_{2,b}$ is x-coordinate of the upper-right corner of the bar, $y_{1,b}$ is y-coordinate of the bottom-left corner of the bar, $y_{2,b}$ is y-coordinate of the upper-right corner of the bar, E_{in} is Young's modulus of inside the bar, and E_{out} is Young's modulus of outside the bar. The bottom-left corner

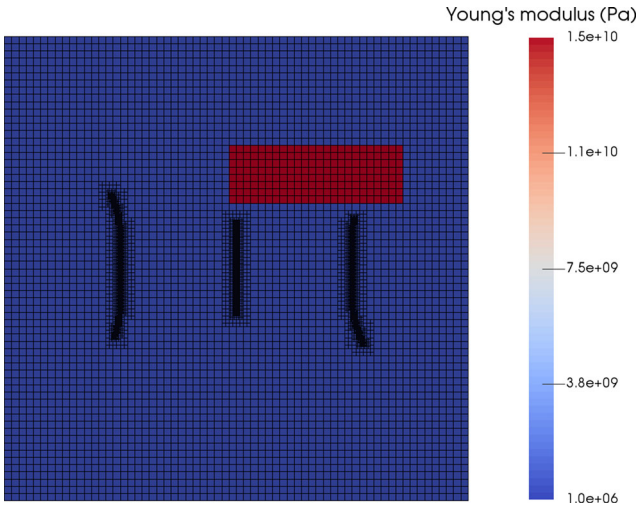

Fig. 13 Example 3. Propagated fractures at time step $n = 250$ with heterogeneous E values of the reference model

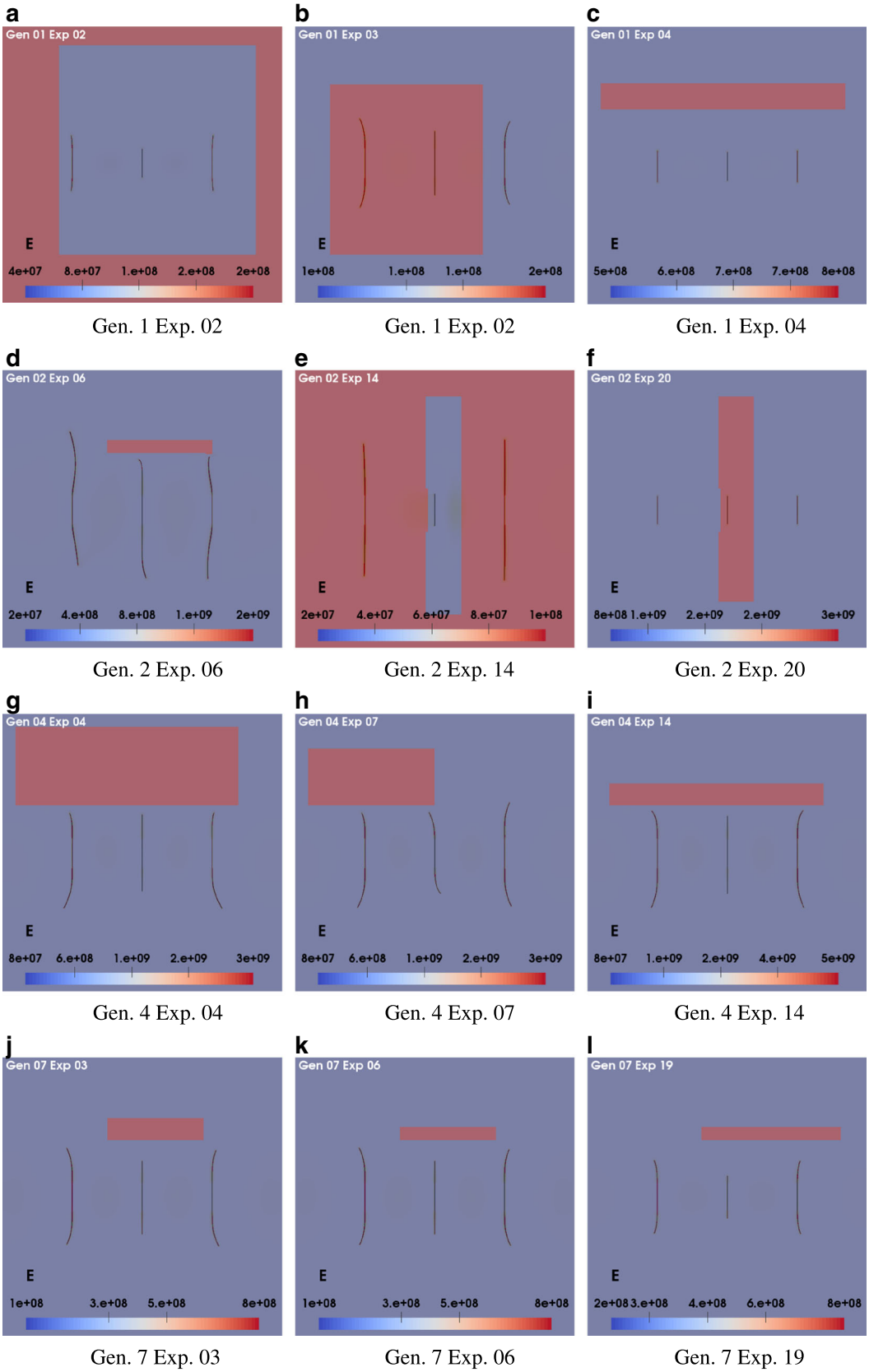

Fig. 14 Example 3. Illustrates the numerical results for selected generations (Gen=1,2,4, and 7) and experiments (Exp.). Each row indicates different generations. We observe a convergence of the solution to the reference model

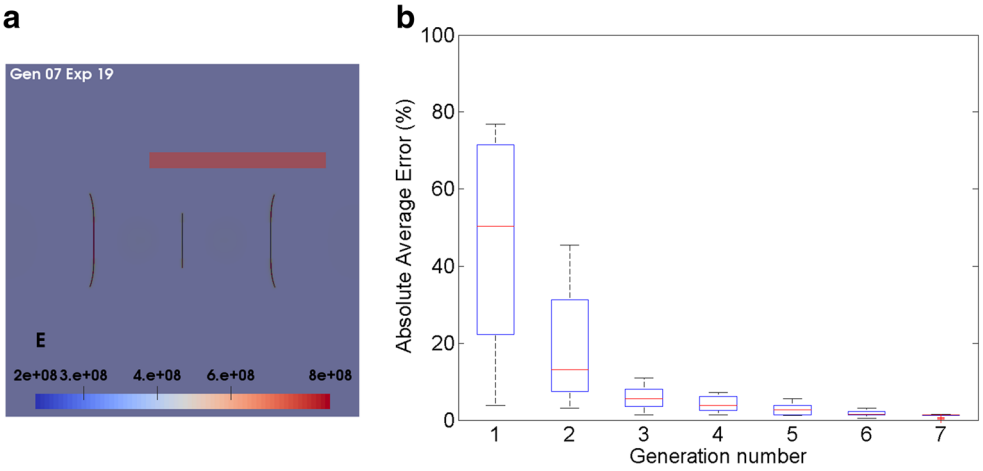

Fig. 15 Example 3. Evolution of objective function values for the history-matching problem: **a** the optimal solution and **b** convergence of objective function values

of the domain is taken to be the origin of the domain. The range of each variable is as follows: $x_{1,b}, x_{2,b} \in [0\,\text{m}, 4\,\text{m}]$; $y_{1,b}, y_{2,b} \in [0\,\text{m}, 4\,\text{m}]$; $E_{in} \in [10^6\ \text{Pa}, 10^{10}\ \text{Pa}]$; and $E_{out} \in [10^7\ \text{Pa}, 10^9\ \text{Pa}]$. We intentionally made genetic algorithm more difficult to converge by giving a wide range for Young's modulus.

The objective function for this example is the absolute average percent error derived from the form of Eq. 31 as

$$\arg\min_{\curvearrowleft \in \mathbb{R}^N} f(\curvearrowleft) = \arg\min_{\curvearrowleft \in \mathbb{R}^6} \frac{1}{N_{obs}} \sum_{i=1}^{N_{obs}} \left| \frac{V_{f,i}^{ref} - V_{f,i}}{V_{f,i}^{ref}} \right| \times 100(\%), \quad (34)$$

where V_f^{ref} is the fracture area of the reference solution that corresponds to $\mathbf{d}^{obs}$ in Eq. 31 and N_{obs} is the number of observations. In this example, $N_{obs} = 1$ as V_f^{ref} measured at the last time step is the only observation data used to calculate the objective function.

Operating parameters of hydraulic fracturing are fixed in all phase field runs: the number of fractures is three, injection rate is constant at each fracture interval, and fracture spacing between the inner fracture and each outer fracture is constant 1 m. At the last time step $n = 250$, the reference model yields the total area of fractures $V_f^{ref} = 0.00974681\,\text{m}^2$, which results from $x_{1,b} = 2.0\,\text{m}$, $x_{2,b} = 3.5\,\text{m}$, $y_{1,b} = 2.5\,\text{m}$, $y_{2,b} = 3.0\,\text{m}$, $E_{in} = 10^{10}$ Pa, and $E_{out} = 10^8$ Pa. Because the Example 3 set up the single bar, it might be reasonable if the solution set converges not only the reference solution but also the following three solutions: $(x_{1,b}, y_{1,b}) = (0.5\text{m}, 2.0\text{m})$, $(x_{2,b}, y_{2,b}) = (2.5\text{m}, 3.0\text{m})$; $(x_{1,b}, y_{1,b}) = (2.0\text{m}, 3.5\text{m})$, $(x_{2,b}, y_{2,b}) = (1.0\text{m}, 1.5\text{m})$; and $(x_{1,b}, y_{1,b}) = (0.5\text{m}, 2.0\text{m})$, $(x_{2,b}, y_{2,b}) = (1.0\text{m}, 1.5\text{m})$.

Figure 14 illustrates the numerical results for selected generations and experiments. Each generation had 20 experiments and 10 generations were tested. Since no conditions between E_{in} and E_{out} were provided, we observed some cases with $E_{in} < E_{out}$ that yielded unfavorable simulation results during earlier generations. After the fourth generation, it seems that most experiments get closer to the reference solution in terms of the position of the bar.

As a consequence, Fig. 15a provides the optimized solution similar to the reference solution shown in Fig. 13. The derived fractures are somewhat symmetric despite the existence of the single bar with the high Young's modulus on the upper part of the domain, but the degree of fracture asymmetry depends on the characteristics of the bar (e.g., size and position). We expect a larger bar enhances the asymmetry more remarkably as seen in Fig. 14d. Also, that kind of asymmetric fractures can be more pronounced if increasing the injection time step . The variance of each variable decreased during the generational process. Interestingly, the thickness of the block $y_{2,b} - y_{1,b}$ was a less crucial factor to the performance of genetic algorithm because the phase field model did not allow fractures to penetrate the bar under the given operating condition. Note that the fracture growth mechanisms in a complex sedimentary basin are dominated by not only heterogeneities of reservoir properties such as material property contrast but also the operating condition [16]. A higher fluid injection rate that can grow fractures with penetrating the bar would reduce the uncertainty related to the thickness of the block by providing more information beyond the bar.

Figure 15b shows the stable decrease in the objective function values from the first to the seventh generations. As most experiments were assimilated in the seventh generation, the results from the eighth to the tenth generations are omitted in this figure. Notwithstanding the small positive absolute average percent error, it seems that all solutions arrive near the global minimum (i.e., reference model) in the seventh generation. Note that this six-dimensional problem requires more expensive computational costs for achieving the convergence towards the

global optimal solution than the two-dimensional problem described in Examples 1 and 2. Employing faster inverse algorithms [8] or coupling a surrogate model with the forward model [51] would contribute to saving computational costs for solving more high-dimensional complex problems. It is also anticipated that reflecting reservoir uncertainty on the parameters adjusted in these examples would deliver more realistic outcomes in future works.

4 Conclusions

This work integrated the phase field fracture propagation model with an optimization tool (UT-OPT) for accomplishing optimal hydraulic fracturing design at unconventional shale oil or gas reservoirs. Genetic algorithm implemented in UT-OPT adjusted fracture intervals for three-stage hydraulic fracturing problems with a single well in a heterogeneous porous media. The operating parameters derived from GA were assigned to the phase field model that estimated the volume (area) of propagated fractures as a performance indicator of hydraulic fracturing. This indicator will be replaced with oil production or net present value after completing the integration of the phase field fracture propagation model with a reservoir simulator. The optimization process was iterated until no further improvements in the objective function were achieved or when the maximum number of iteration was reached. Computational effects of heterogeneity and stress-shadowing effects due to fracture spacing were analyzed with applications to both homogeneous and heterogeneous media. All numerical simulations herein were executed concurrently using a high-performance parallel computing for reducing the computational cost. These results illustrate the capabilities of this integrated algorithm to further apply for more realistic scenarios in petroleum engineering. Coupling the phase field fracture algorithms to the field-scale reservoir simulator, which will enable employing production rate as the objective function, is our ongoing work.

Funding information The research by S. Lee, B. Min, and M. F. Wheeler were funded by the U.S. Department of Energy, National Energy Technology Laboratory grant DOE FG02-04ER25617. S. Lee and M. F. Wheeler were partially supported by NSF grant NSF 1546553. B. Min was funded by the National Research Foundation of Korea (NRF) grants (No. NRF-2017R1C1B5017767, No. NRF-2017K2A9A1A01092734).

References

1. Abass, H.H., Soliman, M.Y., Al-Tahini, A.M., Surjaatmadja, J.B., Meadows, D.L., Sierra, L.: Oriented fracturing: a new technique to hydraulically fracture an openhole horizontal well. In: SPE Annual Technical Conference and Exhibition (2009)
2. Almani, T., Kumar, K., Dogru, A., Singh, G., Wheeler, M.F.: Convergence analysis of multirate fixed-stress split iterative schemes for coupling flow with geomechanics. Comput. Methods Appl. Mech. Eng. **311**, 180–207 (2016)
3. Almani, T., Lee, S., Wheeler, M.F., Wick, T.: Multirate coupling for flow and geomechanics applied to hydraulic fracturing using an adaptive phase-field technique. volume SPE-182610-MS Society of Petroleum Engineers (2017)
4. Ambrosio, L., Tortorelli, V.: Approximation of functionals depending on jumps by elliptic functionals via γ-convergence. Commun. Pure Appl. Math. **43**, 999–1036 (1990)
5. Ambrosio, L., Tortorelli, V.: On the approximation of free discontinuity problems. Unione Matematica Italiana. Bollettino. B. **6**, 105–123 (1992)
6. Amor, H., Marigo, J.-J., Maurini, C.: Regularized formulation of the variational brittle fracture with unilateral contact numerical experiments. J. Mech. Phys. Solids **57**, 1209–1229 (2009)
7. Bangerth, W., Davydov, D., Heister, T., Heltai, L., Kanschat, G., Kronbichler, M., Maier, M., Turcksin, B., Wells, D.: The deal.II library, version 8.4. J. Numer. Math. **24**(3), 135–141 (2016)
8. Bangerth, W., Klie, H., Wheeler, M.F., Stoffa, P.L., Sen, M.K.: On optimization algorithms for the reservoir oil well placement problem. Comput. Geosci. **10**(3), 303–319 (2006)
9. Bourdin, B., Francfort, G., Marigo, J.-J.: Numerical experiments in revisited brittle fracture. J. Mech. Phys. Solids **48**(4), 797–826 (2000)
10. Britt, L.: Optimized oilwell fracturing of moderate-permeability reservoirs. In: SPE Annual Technical Conference and Exhibition (1985)
11. Castonguay, S.T., Mear, M.E., Dean, R.H., Schmidt, J.H.: Predictions of the growth of multiple interacting hydraulic fractures in three dimensions. In: SPE Annual Technical Conference and Exhibition, vol. 3, pp. 2206–2217 (2013)
12. Cheng, C., Bunger, A.P., Peirce, A.P.: Optimal perforation location and limited entry design for promoting simultaneous growth of multiple hydraulic fractures. In: SPE Hydraulic Fracturing Technology Conference (2016)
13. Dean, R., Gai, X., Stone, C., Minkoff, S.: A comparison of techniques for coupling porous flow and geomechanics. SPE-79709-MS, 132–140 (2006)
14. Deb, K., Pratap, A., Agarwal, S., Meyarivan, T.: A fast and elitist multiobjective genetic algorithm: Nsga-ii. IEEE Trans. Evol. Comput. **6**(2), 182–197 (2002)
15. Dohmen, T., Zhang, J.J., Blangy, J.-P.: Stress shadowing effect key to optimizing spacing of multistage fracture stages. American Oil & Gas Reporter (2015)
16. Fisher, M., Warpinski, N.: Hydraulic-fracture-height growth: real data. SPE Prod. Oper. **27**(1), 8–19 (2012)
17. Fisher, M.K., Wright, C.A., Davidson, B.M., Goodwin, A., Fielder, E., Buckler, W., Steinsberger, N.: Integrating fracture mapping technologies to optimize stimulations in the Barnett Shale. In: SPE Annual Technical Conference and Exhibition (2002)
18. Francfort, G., Marigo, J.-J.: Revisiting brittle fracture as an energy minimization problem. J. Mech. Phys. Solids **46**(8), 1319–1342 (1998)
19. Girault, V., Kumar, K., Wheeler, M.F.: Convergence of iterative coupling of geomechanics with flow in a fractured poroelastic medium. Comput. Geosci. **20**(5), 997–1011 (2016). https://doi.org/10.1007/s10596-016-9573-4
20. Goldberg, D.E.: Genetic Algorithms in Search, Optimization and Machine Learning. Addison-Wesley Professional, Reading (1989)
21. Heider, Y., Markert, B.: A phase-field modeling approach of hydraulic fracture in saturated porous media. Mechanics Research Communications (2016)
22. Heister, T., Wheeler, M.F., Wick, T.: A primal-dual active set method and predictor-corrector mesh adaptivity for computing

fracture propagation using a phase-field approach. Comput. Methods Appl. Mech. Eng. **290**, 466–495 (2015)
23. Holditch, S.A., Jennings, J.W., Neuse, S.H., Wyman, R.E.: The optimization of well spacing and fracture length in low permeability gas reservoirs. In: SPE Annual Fall Technical Conference and Exhibition (1978)
24. Holland, J.H.: Adaptation in Natural and Artificial Systems: An Introductory Analysis with Applications to Biology, Control, and Artificial Intelligence. U Michigan Press, Ann Arbor (1975)
25. Karma, A., Kessler, D.A., Levine, H.: Phase-field model of mode iii dynamic fracture. Phys. Rev. Lett. **87**, 045501 (2001)
26. Kim, J., Tchelepi, H., Juanes, R.: Stability, accuracy, and efficiency of sequentiel methods for flow and geomechanics. SPE J. **16**(2), 249–262 (2011)
27. Kim, J., Tchelepi, H., Juanes, R.: Stability and convergence of sequentiel methods for coupled flow and geomechanics: fixed-stress and fixed-strain splits. Comput. Methods Appl. Mech. Eng. **200**(13-16), 1591–1606 (2011)
28. Lee, S., Lee, Y.-J., Wheeler, M.F.: A locally conservative enriched galerkin approximation and efficient solver for elliptic and parabolic problems. SIAM J. Sci. Comput. **38**(3), A1404–A1429 (2016)
29. Lee, S., Mikelić, A., Wheeler, M., Wick, T.: Phase-field modeling of two-phase fluid-filled fractures in a poroelastic medium. submitted (2017)
30. Lee, S., Mikelić, A., Wheeler, M.F., Wick, T.: Phase-field modeling of proppant-filled fractures in a poroelastic medium. Comput. Method Appl. Mech. Eng. **312**, 509–541 (2016). Phase Field Approaches to Fracture
31. Lee, S., Reber, J.E., Hayman, N.W., Wheeler, M.F.: Investigation of wing crack formation with a combined phase-field and experimental approach. Geophys. Res. Lett. **43**(15), 7946–7952 (2016)
32. Lee, S., Wheeler, M.F., Wick, T.: Pressure and fluid-driven fracture propagation in porous media using an adaptive finite element phase field model. Comput. Methods Appl. Mech. Eng. **305**, 111–132 (2016)
33. Lee, S., Wheeler, M.F., Wick, T.: Iterative coupling of flow, geomechanics and adaptive phase-field fracture including level-set crack width approaches. J. Comput. Appl. Math. **314**, 40–60 (2017)
34. Lee, S., Wheeler, M.F., Wick, T., Srinivasan, S.: Initialization of phase-field fracture propagation in porous media using probability maps of fracture networks. Mech. Res. Commun. **80**, 16–23 (2017). Multi-Physics of Solids at Fracture
35. Liu, C.H.: Optimizing Hydraulic Fracture Spacing and Lateral Well Spacing in Tight/Unconventional Resource Development through Fully Coupling Stress Shadowing Effects and Fluid Flow – an Integrated Approach. PhD thesis, Colorado School of Mines (2016)
36. Ma, X., Gildin, E., Plaksina, T.: Efficient optimization framework for integrated placement of horizontal wells and hydraulic fracture stages in unconventional gas reservoirs. J Unconventional Oil Gas Res. **9**, 1–17 (2015)
37. Mauthe, S., Miehe, C.: Hydraulic fracture in poro-hydro-elastic media. Mechanics Research Communications (2016)
38. Meyer, B.R., Bazan, L.W.: A discrete fracture network model for hydraulically induced fractures-theory, parametric and case studies. In: SPE Hydraulic Fracturing Technology Conference (2011)
39. Miehe, C., Hofacker, M., Welschinger, F.: A phase field model for rate-independent crack propagation: robust algorithmic implementation based on operator splits. Comput. Methods Appl. Mech. Eng. **199**, 2765–2778 (2010)
40. Miehe, C., Kienle, D., Aldakheel, F., Teichtmeister, S.: Phase field modeling of fracture in porous plasticity: a variational gradient-extended eulerian framework for the macroscopic analysis of ductile failure. Computer Methods in Applied Mechanics and Engineering (2016)
41. Miehe, C., Welschinger, F., Hofacker, M.: Thermodynamically consistent phase-field models of fracture: variational principles and multi-field fe implementations. Int. J. Numer. Methods Eng. **83**, 1273–1311 (2010)
42. Mikelić, A., Wang, B., Wheeler, M.F.: Numerical convergence study of iterative coupling for coupled flow and geomechanics. Comput. Geosci. **18**(3-4), 325–341 (2014)
43. Mikelić, A., Wheeler, M., Wick, T.: A phase-field approach to the fluid filled fracture surrounded by a poroelastic medium. ICES Report, 13–15 (2013)
44. Mikelić, A., Wheeler, M., Wick, T.: Phase-field modeling of a fluid-driven fracture in a poroelastic medium. In: Press in Computational Geosciences (2013). https://doi.org/10.1007/s10596-015-9532-5
45. Mikelić, A., Wheeler, M.F.: Convergence of iterative coupling for coupled flow and geomechanics. Comput. Geosci. **17**(3), 455–462 (2012)
46. Mikelić, A., Wheeler, M.F., Wick, T.: A phase-field method for propagating fluid-filled fractures coupled to a surrounding porous medium. SIAM Multiscale Model Simul. **13**(1), 367–398 (2015)
47. Mikelić, A., Wheeler, M.F., Wick, T.: A quasi-static phase-field approach to pressurized fractures. Nonlinearity **28**(5), 1371–1399 (2015)
48. Min, B., Kang, J.M., Chung, S., Park, C., Jang, I.: Pareto-based multi-objective history matching with respect to individual production performance in a heterogeneous reservoir. J. Pet. Sci. Eng. **122**, 551–566 (2014)
49. Min, B., Kang, J.M., Lee, H., Jo, S., Park, C., Jang, I.: Development of a robust multi-objective history matching for reliable well-based production forecasts. Energy Explor. Exploit. **34**(6), 795–809 (2016)
50. Min, B., Park, C., Jang, I., Kang, J.M., Chung, S.: Development of pareto-based evolutionary model integrated with dynamic goal programming and successive linear objective reduction. Appl. Soft Comput. **35**, 75–112 (2015)
51. Min, B., Park, C., Kang, J., Park, H., Jang, I.: Optimal well placement based on artificial neural network incorporating the productivity potential. Energy Sources, Part A **33**(18), 1726–1738 (2011)
52. Min, B., Wheeler, M.F., Sun, A.Y.: Parallel multiobjective optimization for the coupled compositional/geomechanical modeling of pulse testing. In: SPE Reservoir Simulation Conference. Society of Petroleum Engineers (2017)
53. Nagel, N., Zhang, F., Sanchez-Nagel, M., Lee, B., Agharazi, A., et al: Stress shadow evaluations for completion design in unconventional plays. In: SPE Unconventional Resources Conference Canada. Society of Petroleum Engineers (2013)
54. Peirce, A., Bunger, A.: Interference fracturing: non-uniform distributions of perforation clusters that promote simultaneous growth of multiple hydraulic fractures. SPE J. **20**(2), 384–395 (2015)
55. Peirce, A., Detournay, E.: An implicit level set method for modeling hydraulically driven fractures. Comput. Methods Appl. Mech. Eng. **197**(33), 2858–2885 (2008)
56. Rice, J.R.: Mathematical analysis in the mechanics of fracture. Fracture: An Advan. Treatise **2**, 191–311 (1968)
57. Saputelli, L., Lopez, C., Chacon, A., Soliman, M.: Design optimization of horizontal wells with multiple hydraulic fractures in the bakken shale. In: SPE/EAGE European Unconventional Resources Conference and Exhibition (2014)
58. Settari, A., Mourits, F.: A coupled reservoir and geomechanical simulation system. SPE J. **3**(3), 219–226 (1998)

59. Singh, G., Pencheva, G., Kumar, K., Wick, T., Ganis, B., Wheeler, M.: Impact of Accurate Fractured Reservoir Flow Modeling on Recovery Predictions. SPE 188630-MS, SPE Hydraulic Fracturing Technology Conference, Woodlands, TX (2014)
60. Veatch, R.: Overview of current hydraulic fracturing design and treatment technology-part 1. J. Petrol. Tech. **35**(4), 677–687 (1983)
61. Vincent, M.: The next opportunity to improve hydraulic-fracture stimulation. J. Petrol. Tech. **64**(3), 118–127 (2012)
62. Wheeler, J., Wheeler, M.: Ipars technical manual. Center for Subsurface Modeling, The University of Texas at Austin (1990)
63. Wick, T., Lee, S., Wheeler, M.F.: 3D phase-field for pressurized fracture propagation in heterogeneous media. VI International Conference on Computational Methods for Coupled Problems in Science and Engineering 2015 Proceedings (2015)
64. Wick, T., Singh, G., Wheeler, M.: Fluid-filled fracture propagation using a phase-field approach and coupling to a reservoir simulator. SPE J. **21**, 981–999 (2015)
65. Wu, K., Olson, J., Balhoff, M.T., Yu, W., et al.: Numerical analysis for promoting uniform development of simultaneous multiple-fracture propagation in horizontal wells. SPE Production & Operations (2016)
66. Wu, K., Olson, J.E., et al.: Investigation of the impact of fracture spacing and fluid properties for interfering simultaneously or sequentially generated hydraulic fractures. SPE Prod. Oper. **28**(04), 427–436 (2013)
67. Wu, K., Olson, J.E., et al.: Mechanisms of simultaneous hydraulic-fracture propagation from multiple perforation clusters in horizontal wells. SPE Journal (2016)
68. Xiong, H.: Optimizing cluster or fracture spacing: an overview (2017)
69. Zangeneh, N., Eberhardt, E., Bustin, R.: Investigation of the influence of stress shadows on horizontal hydraulic fractures from adjacent lateral wells. J Unconventional Oil Gas Res. **9**, 54–64 (2015)